Low Dust Mass and High Star Formation Efficiency at z > 12 from Deep ALMA Observations

The Astrophysical Journal, 1000:159 (11pp), 2026 April 1 https://doi.org/10.3847/1538-4357/ae4511

Low Dust Mass and High Star Formation Efficiency at $z > 12$ from Deep ALMA Observations

Ikki Mitsuhashi[1,2,3], Jorge A. Zavala[3,4], Tom J. L. C. Bakx[5], Akio K. Inoue[2,6], Marco Castellano[7], Antonello Calabrò[7], Caitlin M. Casey[8], Maximilien Franco[8], Bunyo Hatsukade[3,9,10], Nimish P. Hathi[11], Ryota Ikeda[3,12], Anton M. Koekemoer[11], Jeyhan Kartaltepe[13], Kirsten K. Knudsen[14], Paola Santini[7], Toshiki Saito[15], Elena Terlevich[16,17,18], Roberto Terlevich[16,17,18], and L. Y. Aaron Yung[11]

[1] Department for Astrophysical & Planetary Science, University of Colorado, Boulder, CO 80309, USA; ikki0913astr@gmail.com
[2] Waseda Research Institute for Science and Engineering, Faculty of Science and Engineering, Waseda University, 3-4-1 Okubo, Shinjuku, Tokyo 169-8555, Japan
[3] National Astronomical Observatory of Japan, 2-21-1 Osawa, Mitaka, Tokyo 181-8588, Japan
[4] University of Massachusetts Amherst, 710 North Pleasant Street, Amherst, MA 01003-9305, USA
[5] Department of Space, Earth and Environment, Chalmers University of Technology, SE-412 96 Gothenburg, Sweden
[6] Department of Physics, School of Advanced Science and Engineering, Faculty of Science and Engineering, Waseda University, 3-4-1, Okubo, Shinjuku, Tokyo 169-8555, Japan
[7] INAF—Osservatorio Astronomico di Roma, via di Frascati 33, 00078, Monte Porzio Catone, Italy
[8] Department of Astronomy, The University of Texas at Austin, 2515 Speedway Boulevard Stop C1400, Austin, TX 78712, USA
[9] Graduate Institute for Advanced Studies, SOKENDAI, Osawa, Mitaka, Tokyo 181-8588, Japan
[10] Institute of Astronomy, Graduate School of Science, The University of Tokyo, 2-21-1 Osawa, Mitaka, Tokyo 181-0015, Japan
[11] Space Telescope Science Institute, 3700 San Martin Drive, Baltimore, MD 21218, USA
[12] Department of Astronomy, School of Science, SOKENDAI (The Graduate University for Advanced Studies), 2-21-1 Osawa, Mitaka, Tokyo 181-8588, Japan
[13] Laboratory for Multiwavelength Astrophysics, School of Physics and Astronomy, Rochester Institute of Technology, 84 Lomb Memorial Drive, Rochester, NY 14623, USA
[14] Department of Earth and Space Sciences, Chalmers University of Technology, Onsala Space Observatory, SE-43992 Onsala, Sweden
[15] Faculty of Global Interdisciplinary Science and Innovation, Shizuoka University, 836 Ohya, Suruga-ku, Shizuoka 422-8529, Japan
[16] Instituto Nacional de Astrofísica, Óptica y Electrónica, Tonantzintla, AP 51 y 216, 72000, Puebla, Mexico
[17] Institute of Astronomy, University of Cambridge, Cambridge, CB3 0HA, UK
[18] Facultad de Astronomía y Geofísica, Universidad de La Plata, FWA, B1900 La Plata, Argentina
Received 2024 December 20; revised 2026 February 9; accepted 2026 February 10; published 2026 March 20

Abstract

We investigate the dust mass buildup and star formation efficiency of two galaxies at $z > 12$—GHZ2 and GS-z14-0—by combining Atacama Large Millimeter/submillimeter Array and JWST observations with an analytical model that assumes dust at thermal equilibrium. We obtained 3σ constraints on the dust mass of $\log M_{\rm dust}/M_{\odot} < 5.0$ and <5.3, respectively. These constraints are in tension with a high dust condensation efficiency in stellar ejecta but are consistent with models with a short metal accretion timescale at $z > 12$. Given the young stellar ages of these galaxies ($t_{\rm age} \sim 10$ Myr), dust grain growth via accretion may still be ineffective at this stage, though it likely works efficiently to produce significant dust in galaxies at $z \sim 7$. The star formation efficiencies, defined as the star formation rate divided by the molecular gas mass, reach $\sim$10 Gyr^{-1} over a 10 Myr timescale, aligning with the expected redshift evolution of "starburst" galaxies with efficiencies that are $\sim$0.5–1 dex higher than those in main-sequence galaxies. This starburst phase seems to be common in UV-bright galaxies at $z > 12$ and is likely associated with the unique conditions of the early phases of galaxy formation, such as bursty star formation. Direct observations of molecular gas tracers like [C II] will be crucial to further understanding the nature of bright galaxies at $z > 12$.

Unified Astronomy Thesaurus concepts: Galaxy evolution (594); Galaxy formation (595); High-redshift galaxies (734); Dust formation (2269)

1. Introduction

Dust and gas are fundamental components of the interstellar medium (ISM). Gas is the primary fuel for star formation, and dust plays a key role in rapidly cooling this component to facilitate the collapse of gas clouds into stars. Cosmic dust originates from stellar phenomena, such as the ejecta of asymptotic giant branch (AGB) stars and rapidly cooling supernova (SN) ejecta (E. Dwek & J. M. Scalo 1980; P. Todini & A. Ferrara 2001; T. Nozawa et al. 2007). The dust produced by stellar activity ("stellar dust") grows in the dense ISM through metal accretion and condensation into dust grains ("ISM dust"; e.g., B. T. Draine 1990, 2009; A. K. Inoue 2011; S. Zhukovska 2014). Therefore, the dust content within galaxies is directly connected to the star formation history (SFH) and the metal enrichment process.

The formation and growth of interstellar dust have been studied in relation to other galactic properties, such as the stellar mass, gas mass, and metallicity (L. Ciesla et al. 2014; P. Santini et al. 2014; E. da Cunha et al. 2015; M. Mancini et al. 2015). The dust-to-gas mass ratio (D/G) represents the fraction of dust relative to the ISM, serving as a powerful tool for investigating dust growth. In the local Universe, D/G has been intensively investigated over the past decades (e.g., J. Koornneef 1982; M. R. Issa et al. 1990; H. Hirashita et al. 2002; G. J. Bendo et al. 2010; L. Magrini et al. 2011) and found to be correlated with metallicity (Z) across a large

dynamical range (U. Lisenfeld & A. Ferrara 1998; B. T. Draine et al. 2007; A. K. Leroy et al. 2011; A. Rémy-Ruyer et al. 2014), which may reflect both chemical evolution and dust grain growth (E. Dwek 1998; F. Galliano et al. 2008; R. S. Asano et al. 2013; G. Popping et al. 2017; L. Graziani et al. 2020). Constraining D/G at high redshift is especially important, as the Universe's young age limits the contribution of several prominent dust production processes (e.g., G. E. Magdis et al. 2012; G. Popping et al. 2023; M. Palla et al. 2024; F. Valentino et al. 2024; A. Ferrara et al. 2025a).

Recent Atacama Large Millimeter/submillimeter Array (ALMA) studies have found a substantial amount of dust in galaxies at $z = 6$–8 (N. Laporte et al. 2017; Y. Tamura et al. 2019; H. Inami et al. 2022; J. Witstok et al. 2023a). Several scenarios have been considered to account for this significant dust mass at this early epoch, such as high-dust-condensation efficiency or efficient metal accretion into the ISM (Q. Li et al. 2019; H.-M. Liu & H. Hirashita 2019; L. Graziani et al. 2020; P. Dayal et al. 2022; J. Witstok et al. 2023b; D. Burgarella et al. 2024). Investigation of the emergence of dust in more distant galaxies is essential for understanding the rapid increase in dust mass in the early Universe and identifying the main processes that contribute to this growth (e.g., D. Burgarella et al. 2024). The small age of the Universe further helps explore the rapid pathways that drive dust growth.

Beyond D/G, the total (or molecular) gas mass also provides valuable insights, as stars form from molecular gas via various cooling mechanisms, including dust thermal emission. Specifically, the star formation efficiency (SFE), defined as the star formation rate (SFR) divided by molecular gas mass, indicates how galaxies convert gas into stars and how gas is depleted by feedback (see L. J. Tacconi et al. 2020 for a review). Observations of molecular gas tracers such as CO and [C II] lines have shown that galaxies on the star-forming main sequence (MS) typically exhibit lower SFE than "starburst" (SB) galaxies (e.g., D. B. Sanders et al. 1991; M. T. Sargent et al. 2012; L. J. Tacconi et al. 2018). For instance, M. Dessauges-Zavadsky et al. (2020) reported a weak redshift evolution of the gas depletion timescale ($t_{\rm dep} \propto 1/{\rm SFE}$) in UV-selected galaxies, suggesting moderate star formation activity complemented by significant outflows that remove the gas present for future cycles of star formation up to $z \sim 5$. This trend is also confirmed at $z \sim 7$ (M. Aravena et al. 2024). While it is unclear whether there would be any further evolution in the earlier 400 Myr of cosmic time, it could be a key probe to investigate the origin of the overabundance of UV-bright galaxies at $z > 12$ (e.g., M. Castellano et al. 2022; H. Atek et al. 2023; Y. Harikane et al. 2023; S. L. Finkelstein et al. 2024; L. Y. A. Yung et al. 2024).

In this paper, we examine the ISM of two $z > 12$ galaxies using ultradeep ALMA observations of the [O III] emission and the dust continuum. Our study focuses on two of the highest-redshift galaxies known to date: GHZ2 at $z = 12.3$ (M. Castellano et al. 2024; J. A. Zavala et al. 2025) and GS-z14-0 at $z = 14.2$ (S. Carniani et al. 2024). Leveraging the gas-phase and stellar metallicities as well as stellar assembly histories observed at $z > 12$, which have been available thanks to the exceptional sensitivity of the James Webb Space Telescope (JWST), we aim to explore the dust production, dust growth, and SFE in these early galaxies by exploiting the available deep ALMA observations.

The paper is organized as follows. Section 2 provides an overview of the datasets used in this work. Section 3 describes the method of dust mass measurements. In Section 4, we discuss the dust production, growth, and destruction at $z > 12$ based on our constraints on the M_*–$M_{\rm dust}$ relation, the Z–D/G relation, and the dust production history, as well as the SFE of the targeted galaxies. The conclusions are presented in Section 5. Throughout this paper, we assume a flat Universe with the cosmological parameters of $\Omega_{\rm M} = 0.3$, $\Omega_\Lambda = 0.7$, $\sigma_8 = 0.8$, and $H_0 = 70\,{\rm km\,s^{-1}\,Mpc^{-1}}$.

2. Targets

In this section, we summarize the observed and inferred properties of the two target galaxies. While the spectral energy distribution (SED) modeling of the two galaxies is not identical, as detailed below—e.g., the mass range of the initial mass function (IMF) to be integrated or the assumption of the nonparametric SFH—we have applied the best available values wherever possible. Note that some estimations remain uncertain, mainly due to the observational limitations. For instance, further observations covering rest-frame optical wavelengths are necessary to better constrain the stellar masses of galaxies at $z > 10$.

2.1. GHZ2

GHZ2 was originally discovered by JWST photometry as part of the GLASS-JWST Program (T. Treu et al. 2022) and identified in several studies as a robust candidate of the brightest galaxy at $z > 11$ based on its significant Lyα break (M. Castellano et al. 2022; R. P. Naidu et al. 2022; R. Bouwens et al. 2023; Y. Harikane et al. 2023). Its spectroscopic redshift was confirmed to be $z = 12.3$, thanks to the detection of rest-frame UV/optical emission lines with JWST/NIRSpec (M. Castellano et al. 2024) and JWST/MIRI (J. A. Zavala et al. 2025). More recently, J. A. Zavala et al. (2024) reported a detection of [O III]88μm at the $\sim 5\sigma$ level and provided a more accurate redshift ($z = 12.3327 \pm 0.0005$). Both NIRSpec and MIRI constrained its metallicity to be as low as ($Z_{\rm gas}/Z_\odot \sim 0.1$; see also A. Calabro et al. 2024) and, across this paper, we will adopt the reported value of $Z_{\rm gas}/Z_\odot = 0.05^{+0.12}_{-0.03}$ from the line diagnostics in J. A. Zavala et al. (2025). The inferred stellar mass changes depending on the SED fitting code and associated assumptions, with a range of $\log M_*[M_\odot] = 8.3$–8.9 (see the Appendix in J. A. Zavala et al. 2025) after lens magnification correction of $\mu = 1.3$[19] (P. Bergamini et al. 2023). Throughout this paper, we will adopt the SFH derived by BAGPIPES (A. C. Carnall et al. 2018), with a total stellar mass of $\log M_*[M_\odot] = 8.27^{+0.23}_{-0.18}$, owing to its nonparametric approach and good agreement with the PROSPECTOR (B. D. Johnson et al. 2021) results, in Y. Harikane et al. (2025; see Figure 4), which also adopted a nonparametric SFH. Note that despite the rich dataset, it is still unclear whether an active galactic nucleus (AGN) contributes to the UV emission of GHZ2 (see also A. Calabro et al. 2024). And while J. A. Zavala et al. (2024) concluded that this galaxy is likely dominated by star formation activity, based on the [O III]88 μm line width and

[19] While the gravitational lens magnification factor might be up to $\mu \sim 1.6$, due to the closest galaxy at $z = 1.678$, we adopt $\mu = 1.3$ throughout this paper, following J. A. Zavala et al. (2024).

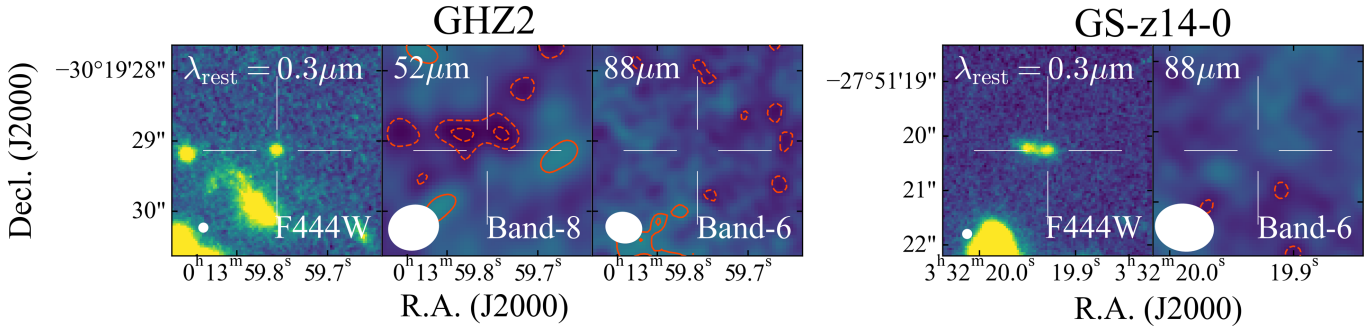

Figure 1. JWST NIRCam F444W and ALMA Band-6/Band-8 thumbnails of GHZ2 in the rest-frame 0.3 μm, 52 μm, and 88 μm continua (left) and GS-z14-0 in the rest-frame 0.3 μm and 88 μm continua (right). The contour levels are shown at $\pm 2\sigma$, $\pm 3\sigma$, $\pm 5\sigma\cdots$ and at increments of 2σ after $\pm 5\sigma$. At the positions of the detection in $\lambda_{\rm rest} = 0.3$ μm, the dust continua remain undetected for both galaxies.

Hβ line luminosity, further observations are necessary to accurately constrain the stellar mass and potential AGN activity in GHZ2.

2.2. GS-z14-0

GS-z14-0 was identified in the JADES NIRCam dataset (B. Robertson et al. 2024) and spectroscopically confirmed via a significant detection of the Lyα break with NIRSpec/PRISM (S. Carniani et al. 2024). Recent ALMA observations reported a successful [O III]88 μm detection at $\sim$6.6σ (S. Carniani et al. 2025; S. Schouws et al. 2025b) and confirmed at $z = 14.1796 \pm 0.0007$. We will refer to the SFH with a stellar mass of $\log M_*[M_\odot] = 8.29^{+0.14}_{-0.09}$ (after magnification correction; $\mu = 1.17$) and the stellar/gas metallicity of $Z/Z_\odot = 0.17^{+0.01}_{-0.01}$ from the PROSPECTOR fitting in S. Carniani et al. (2025) under the nonparametric SFH, which is consistent with the metallicity derived in S. Schouws et al. (2025b). For a conservative discussion, we added $\Delta \log Z = 0.2$, a typical uncertainty in the metallicity estimation at $z \gtrsim 6$ (e.g., K. Nakajima et al. 2023; M. Curti et al. 2024).

3. Data and Analysis

3.1. ALMA Data

ALMA observations of GHZ2 were obtained in both Band 6 and Band 8 by two Director's Discretionary Time (DDT) programs (2021.A.00020.S, PI: Bakx; and 2023.A.00017.S, PI: Zavala), where the spectral setups were designed to cover the [O III]88 μm and the [O III]52 μm lines, respectively. GS-z14-0 has also been observed by ALMA as part of a DDT program (2023.A.00037.S, PI: Schouws) targeting the [O III] 88 μm emission line in Band 6. The calibration of the ALMA data is described in detail in J. A. Zavala et al. (2024; see also T. J. L. C. Bakx et al. 2023; S. Carniani et al. 2025); here, we briefly summarize it. The data were calibrated following the standard ALMA pipeline workflow, using CASA version 6.5.1 (CASA Team et al. 2022). After removing channels ± 300 km s^{-1} around the detected [O III]88 μm and expected [O III]52 μm line frequencies, we created continuum images with a natural weighting to maximize the signal-to-noise ratio (S/N). We simply used a dirty image without a primary beam correction, because the S/Ns of our target lines are not expected to be high enough to require the CLEANing procedure, and we require uniform noise distribution within a field of view. The achieved rms levels for GHZ2 and GS-z14-0 data are 3.4 μJy beam^{-1} and 5.0 μJy beam^{-1} with beam sizes of $0\farcs51 \times 0\farcs43$ and $0\farcs82 \times 0\farcs66$ in Band 6 before lens magnification correction, respectively. For GHZ2, the Band-8 observations have an rms depth of 54.6 μJy beam^{-1} with a beam size of $0\farcs71 \times 0\farcs63$, which is much shallower than the Band-6 depth and less constraining on $M_{\rm dust}$, even when taking the $T_{\rm dust}$ variation into account.

Figure 1 shows thumbnails in the rest-frame 0.3 μm and 88 μm (and 52 μm for GHZ2) continua taken by JWST and ALMA. None of the dust continua were detected even with $\gtrsim$7 hr on-source integrations.

3.2. M_{dust} Measurement

We constrain the dust mass of these galaxies by applying an analytical model from A. K. Inoue et al. (2020; hereafter, I20) to the deep ALMA observations. I20 proposed an algorithm to determine the dust mass ($M_{\rm dust}$) and temperatures ($T_{\rm dust}$) under the assumption of radiative equilibrium. In their model, the dust temperature relates to the input radiation source from young stars and the cosmic microwave background (CMB) that is absorbed by dust. Then, by incorporating dust geometry, we can calculate the escape probability of UV photons from the ISM, which results in observable UV luminosities. Among the three available models for the dust geometry provided in I20 (see also N. Imara et al. 2018), we specifically employed the "clumpy" geometry, as it is considered a reliable approximation for high-z galaxies (e.g., Y. Fudamoto et al. 2023; M. Kohandel et al. 2023). Indeed, this "clumpy" geometry provided looser constraints on $M_{\rm dust}$ than the other geometries in I20—i.e., "spherical" or "shell" under the same assumptions—and therefore our analysis is considered to be conservative. To make a direct comparison with previous high-z observational studies (e.g., L. Sommovigo et al. 2022a; J. Witstok et al. 2022; Y. Fudamoto et al. 2023; F. Valentino et al. 2024) and models (e.g., G. Popping et al. 2017; N. Imara et al. 2018), we assumed the dust to be optically thin, with an emissivity index of $\beta_{\rm dust} = 2.0$ (C. M. Casey 2012; E. da Cunha et al. 2021). We also assume a mass absorption coefficient of $\kappa_{\rm UV} = 5.0 \times 10^4$ cm^2 g^{-1}, dust emissivity of $\kappa_0 = 30$ cm^2 g^{-1} at 100 μm, and a clumpiness parameter of $\log \xi_{\rm cl} = -1.0$, following I20 and Y. Fudamoto et al. (2023). The only input from the observations, beyond the continuum flux density, is the spatial extent of the dust. Here, we adopt the spatial extent of the stars traced by the NIRCam photometry as that of the dust-emitting regions ($r_{e,\rm dust} = r_{e,\rm UV}$; see Table 1). Note that in the case of GHZ2, if we use the effective radius of $r_{e,\rm UV} = 39 \pm 10$ pc from Y. Ono et al. (2023), instead of 105 ± 9 pc, the $M_{\rm dust}$ and $M_{\rm gas}$ constraints become tighter than the fiducial values owing to

Table 1
Physical Parameters of Two $z > 12$ Galaxies

	GHZ2	GS-z14-0	References
$M_{\rm UV}$ [mag]	-20.53 ± 0.01	-20.81 ± 0.16	(1, 2)
μ	1.3[a]	1.17	(1, 2)
$r_{e,\rm F200W}$ [pc]	105 ± 9	260 ± 20	(3, 2)
$\log M_*$ [$M_\odot$]	$8.27^{+0.23}_{-0.11}$	$8.29^{+0.14}_{-0.09}$	(4, 2)
$\log M_{\rm dyn}$ [$M_\odot$]	8.9 ± 0.2	8.9 ± 0.2[b]	(5, 2)
$\rm SFR_{10Myr}$ [$M_\odot$ yr^{-1}]	$8.7^{+1.4}_{-1.9}$	$9.9^{+2.3}_{-2.7}$	(4, 6)
$\rm SFR_{100Myr}$ [$M_\odot$ yr^{-1}]	$1.4^{+2.0}_{-0.3}$	$5.6^{+1.2}_{-1.3}$	(4, 6)
$S_{88\mu\rm m}$ [μJy beam^{-1}][c]	<10.3 (3.4)	<14.9 (5.0)	(7)
$S_{52\mu\rm m}$ [μJy beam^{-1}][c]	<163.9 (54.6)	…	(7)
$\log M_{\rm dust}$ [$M_\odot$][d]	<5.0	<5.3	(7)
$\log M_{\rm gas}$ [$M_\odot$]	8.8 ± 0.3	8.7 ± 0.3	(7)

Notes. Every parameter—except for the ALMA observational constraints—is corrected for magnification, as shown in the second row.
[a] As described in J. A. Zavala et al. (2025), the magnification for GHZ2 might be ∼1.6 if we take into account the closest galaxy at $z = 1.682$.
[b] To obtain a consistent $M_{\rm dyn}$ estimation, we uniformly apply Equation (1) in J. A. Zavala et al. (2024; see the text).
[c] 3σ upper limits with 1σ uncertainties, without correcting the magnification.
[d] 3σ upper limits on the dust masses assuming the thermal equilibrium model in I20.
References. (1) M. Castellano et al. (2024); (2) S. Carniani et al. (2024); (3) L. Yang et al. (2022); (4) J. A. Zavala et al. (2025); (5) J. A. Zavala et al. (2024); (6) S. Carniani et al. (2025); and (7) This work.

higher $T_{\rm dust}$ and smaller $M_{\rm dyn}$, respectively. Hence, the results presented here are considered to be conservative.

In Figure 2, we show the resulting $T_{\rm dust}$ and $M_{\rm dust}$ parameter sets acceptable in our calculations based on the I20 model, with observational constraints corrected for gravitational magnification ($\mu = 1.3$ and $\mu = 1.17$ for GHZ2 and GS-z14-0, respectively). Here, in addition to the CMB being considered as a heating source of dust in the I20 model, we took into account the effect of the CMB as a background against the submillimeter emission from a galaxy (e.g., E. da Cunha et al. 2015; H. S. B. Algera et al. 2024). The upper limits on $M_{\rm dust}$ are shown at the intersection between the analytical predictions (thick black dashed line) and the observational limits (red dashed line). Our calculations support very high $T_{\rm dust}$ (>90 K), due to the compact distribution and strong UV radiation. A similarly high $T_{\rm dust}$ was also inferred for a $z \sim 10$ galaxy based on recent ALMA observations (I. Yoon et al. 2023). Metal-poor ISM conditions in the target galaxies may also contribute to these elevated dust temperatures (Y. Tamura et al. 2019; T. J. L. C. Bakx et al. 2020; L. Sommovigo et al. 2022a; I. Mitsuhashi et al. 2024).

As a consequence of the high-dust-temperature conditions, our fitting set a tight 3σ upper limit on the dust masses of $\log M_{\rm dust}/M_\odot < 5.0$ and <5.3 for GHZ2 and GS-z14-0, respectively. These upper limits agree well with the expected dust extinction ($A_V \lesssim 0.5$ mag) under the "clumpy" dust geometry for each $M_{\rm dust}$ calculated through the escaped/intrinsic UV radiation. In addition, the mass constraints are in good agreement with those obtained by A. Ferrara et al. (2025b), where they adopt the SED-based extinction as a proxy of the dust mass. Under the inferred high-$T_{\rm dust}$ conditions, observations at shorter wavelengths are essential for placing tighter constraints on $M_{\rm dust}$. Specifically, we found that utilizing rest frame 25 μm, which is redshifted to ∼350 μm and is observable in ALMA Band 10, would improve the constraints by ∼0.3 dex.

4. Results and Discussion

4.1. Dust Production and Evolution at Cosmic Dawn

In the left panel of Figure 4, we compare our constraints on the dust mass and stellar mass relation with previous constraints for galaxies at $z = 4$–7 (T. J. L. C. Bakx et al. 2021; L. Sommovigo et al. 2022a, 2022b; J. Witstok et al. 2022; F. Valentino et al. 2024). Our results indicate lower dust content in galaxies at $z > 12$ compared to those at $z = 4$–7, a trend that persists when compared with samples from Y. Fudamoto et al. (2023), which were derived using a similar methodology. This conclusion holds even when assuming $T_{\rm dust} = 50$ K (e.g., L. Sommovigo et al. 2022a, 2022b; I. Mitsuhashi et al. 2024), implying a dust mass limit about ∼1 dex larger than our fiducial value, as shown in Figure 3. A recent study by D. Burgarella et al. (2024) suggested a potential decrease in the dust-to-stellar mass ratio at $z > 10$, which is in line with our conclusion. Also, JWST studies of the UV slope $\beta_{\rm UV}$ have supported the small dust influence at $z > 10$ (e.g., F. Cullen et al. 2023, 2024; D. Austin et al. 2025).

The dust-to-stellar mass ratio ($M_{\rm dust}/M_*$) is likely influenced by grain growth within the ISM, which is driven by the condensation of metals in dense gas and is thus inversely proportional to the gas-phase metallicity (e.g., M. de Bennassuti et al. 2014; D. Burgarella et al. 2024). Given the positive correlation between the stellar mass and gas-phase metallicity (i.e., the mass–metallicity relation), grain growth becomes effective around stellar masses of $\log M_*/M_\odot \gtrsim 8.5$ (M. Mancini et al. 2015). Models that assume very efficient grain growth due to enhanced gas condensation do not align closely with the nondetection of dust continua at $z > 12$ (G. Popping et al. 2017; A. P. Vijayan et al. 2019).

In the left panel of Figure 3, we also plot several (semi) analytical models of dust production at $z > 6$ (G. Popping et al. 2017; N. Imara et al. 2018; A. P. Vijayan et al. 2019; C. Di Cesare et al. 2023; V. Mauerhofer & P. Dayal 2023), which predict the dust content evolution due to production by stars, destruction by SNe, and grain growth in clouds. These models reproduce observed trends and scatter well at $z = 4$–7, though most seem to overestimate our measurements at $z > 12$, potentially because their models focus on galaxies at $z \sim 7$–9.

As described in G. Popping et al. (2017), D/G as a function of metallicity is determined by the balance of condensation efficiency ($f_{\rm cond}$) and accretion timescale ($\tau_{\rm acc}$), since both condensation and accretion promote increased D/G. Although the calculations in G. Popping et al. (2017) are up to $z \sim 9$, the fiducial $f_{\rm cond}$ model is much closer to the observational constraints than the high-$f_{\rm cond}$ model. Therefore, the upper limits support a small $f_{\rm cond}$ model rather than the high-efficiency model at $z > 10$. In H.-M. Liu & H. Hirashita (2019), the high-$f_{\rm cond}$ model predicts a large dust mass at the very early stage of galaxy formation (≲10 Myr), while the short-$\tau_{\rm acc}$ model implies a rapid increase of dust mass at the age of ∼100 Myr. If our target galaxies are progenitors of these $z \sim 7$ massive galaxies, small dust amounts at $z > 12$ support the short-$\tau_{\rm acc}$ model with $\tau_{\rm acc} \sim$ 5–100 Myr (H.-M. Liu & H. Hirashita 2019), as the high-$f_{\rm cond}$ model is not preferred.

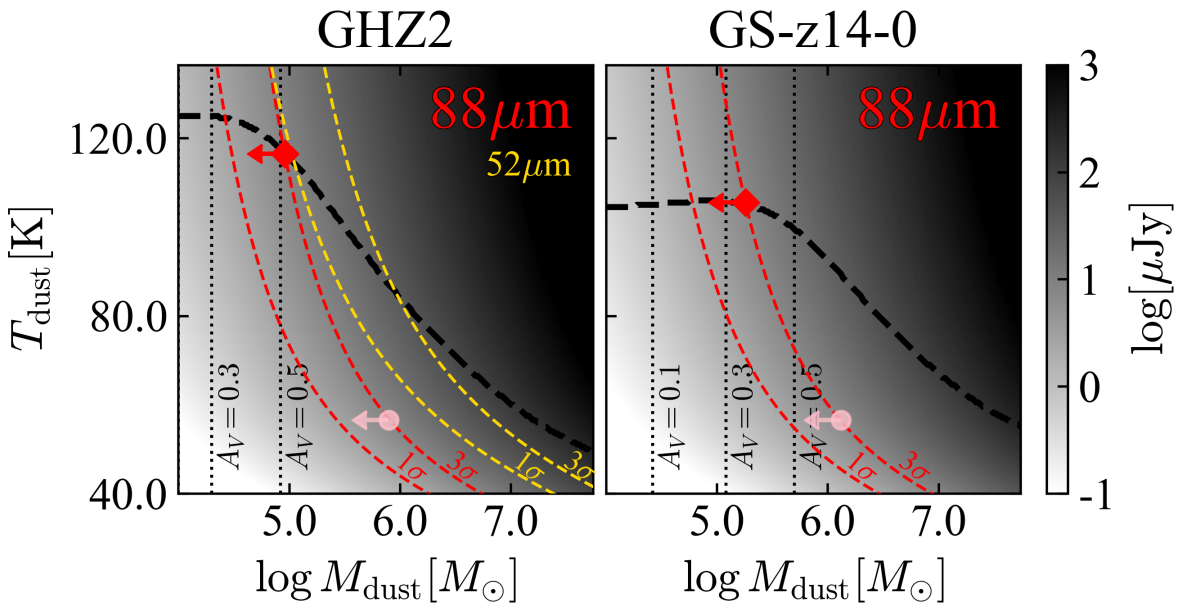

Figure 2. Dust mass and temperatures, color-coded by the S/N of the dust continuum that is expected at rest frame 88 μm for GHZ2 (left) and GS-z14-0 (right). The red solid lines indicate 1σ and 3σ upper limits at rest frame 88 μm, by assuming a modified blackbody spectrum after lens magnification correction. The yellow lines in the left panel show upper limits from rest frame 52 μm, which provides a much less stringent constraint than those derived from rest frame 88 μm. The acceptable parameter sets and derived dust extinction obtained from the I20 model with the clumpy dust geometry are overlaid in the black dashed lines and dotted lines, respectively. Our constraints based on the I20 model are shown with the red diamonds in the cross section of the 3σ red solid lines and black dashed lines. We also illustrated the 3σ upper limit under the assumption of $T_{\rm dust} = 50$ K in the pink circles, just to demonstrate how the I20 model gives tight constraints. Note also that these dust mass constraints do not agree with the observed A_V values (contrary to the values inferred using the I20 model).

Another possible reason for the low dust content at $z > 12$ is that dust is expelled or lifted off by the radiation-driven outflows (A. Ferrara 2024; A. Ferrara et al. 2025a). In their model, the super-Eddington star formation occurs with significant radiation pressure. In this case, the total dust mass might be underestimated, because such expelled dust is no longer in equilibrium. Indeed, GHZ2 and GS-z14-0 are found to have specific SFRs (sSFRs) of log sSFR [Gyr] $\sim$ 1.67 and log sSFR [Gyr] $\sim$ 1.87, respectively, which exceed the critical sSFR (log sSFR [Gyr] $\sim$ 1.4) presented in A. Ferrara (2024). Such a radiation-driven outflow may play an important role in nondetections of the dust continuum.

In the right panel of Figure 3, we explore the relationship between gas-phase metallicity ($Z_{\rm gas}$) and D/G. The constraints on D/G at low-metallicity values are critical for disentangling dust growth scenarios. Here, we computed the gas mass by subtracting the magnification-corrected stellar mass from the dynamical mass ($M_{\rm gas} = M_{\rm dyn}$–$M_*$), assuming negligible dark matter contribution within galaxy centers ($\lesssim r_e$). To obtain a consistent $M_{\rm dyn}$ estimation, we uniformly applied Equation (1) in J. A. Zavala et al. (2024) with [O III]88 μm line widths and increased the 1σ uncertainty by 30%, corresponding to a difference of a factor of $K(n)K(q)$ in Equation (1) of S. Carniani et al. (2025) and a factor of 5 in Equation (1) of J. A. Zavala et al. (2024). For GHZ2 and GS-z14-0, the resulting gas masses in our fiducial calculation are $M_{\rm gas} = 5.8^{+4.4}_{-4.2} \times 10^8\,M_\odot$ and $M_{\rm gas} = 5.4^{+4.1}_{-4.0} \times 10^8\,M_\odot$, respectively. These derived gas masses are broadly consistent with those from their SFRs and the Kennicutt–Schmidt relation ($\sim 6.5 \times 10^8 M_\odot$; R. C. Kennicutt 1998; R. C. Kennicutt & M. A. C. De Los Reyes 2021).

It is worth noting that the mass of the ionized gas component ($M_{\rm ion}$) is smaller than the estimated gas masses. Based on the $L_{\rm H\beta}$–$M_{\rm ion}$ relation presented in R. Chávez et al. (2014), GHZ2 has $M_{\rm ion} = 2.5 \times 10^6$–$9.8 \times 10^7\,M_\odot$ from the Hβ flux of $F_{\rm H\beta} = 0.9 \pm 0.2 \times 10^{-18}$ erg s^{-1} cm^{-2} and an electron density of $n_e = 100$–4000 cm^{-3} (J. A. Zavala et al. 2025). GS-z14-0 is expected to have $M_{\rm ion} = 3.0 \times 10^5$–$1.2 \times 10^7\,M_\odot$ from $F_{\rm H\beta} = 7.9^{+0.17}_{-0.18} \times 10^{-19}$ erg s^{-1} cm^{-2} (J. M. Helton et al. 2025), assuming the same range of electron density as GHZ2.

We obtained constraints of D/G $\lesssim 10^{-4}$ at $Z \sim 0.1\,Z_\odot$ and D/G $\lesssim 10^{-3.5}$ at $Z \sim 0.2\,Z_\odot$. Given the large uncertainty of our constraints, it is difficult to unravel the grain-size distribution (or the accretion timescale, $t_{\rm acc}$) from the Z–D/G relation. In the right panel of Figure 3, we compare our target galaxies with the local dwarf galaxies SBS0335-052 and I Zw 18 (R. Schneider et al. 2016). These two galaxies show a dramatic difference in D/G at similar gas-phase metallicity. R. Schneider et al. (2016) found that the ISM density causes this variety, because of the efficient grain growth in the high-density ISM. Further investigation of the ISM density—such as the molecular gas density (or electron density as a proxy)—might be helpful for confirming the potentially inefficient dust grain growth of galaxies at $z > 12$.

Here, we emphasize the importance of direct observations of molecular gas tracers. In the right panel of Figure 3, we also illustrate the acceptable D/Gs based on $M_{\rm gas}$, assuming gas mass fractions of $f_{\rm gas} = M_{\rm gas}/(M_{\rm gas} + M_*) = 0.1$, 0.5, and 0.9 instead of those from $M_{\rm dyn}$–M_*. Nevertheless, it is impossible to disentangle any models with this broad $f_{\rm gas}$ range of 0.1–0.9. Further ALMA observations targeting [C II] or CO lines will be key to directly constraining $f_{\rm gas}$ and confirming the gas mass

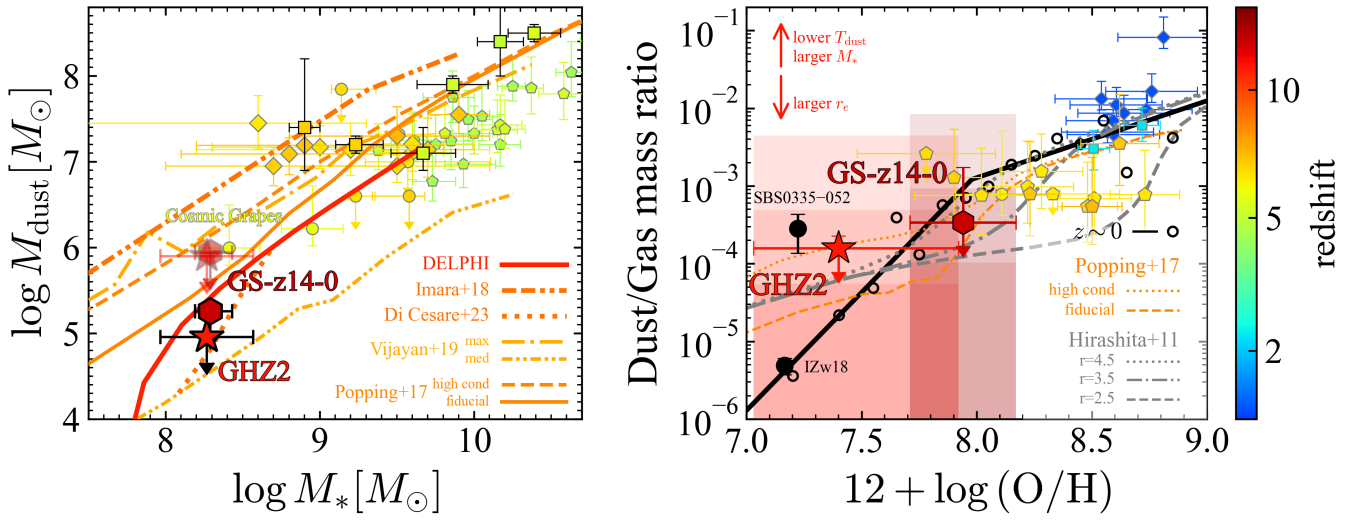

Figure 3. Left: dust mass as a function of the stellar mass. Our constraints for the galaxies at $z > 12$, along with the previous constraints at $z = 4$–8 (T. J. L. C. Bakx et al. 2021; L. Sommovigo et al. 2022a, 2022b; J. Witstok et al. 2022; Y. Fudamoto et al. 2023; F. Valentino et al. 2024) and (semi)analytical models (G. Popping et al. 2017; N. Imara et al. 2018; A. P. Vijayan et al. 2019; C. Di Cesare et al. 2023), including the DELPHI model (V. Mauerhofer & P. Dayal 2023), are shown in colors corresponding to their redshift. For the G. Popping et al. (2017) and A. P. Vijayan et al. (2019) models, predictions with different dust condensation efficiencies are shown with the different line styles. The markers surrounded by black lines are constraints using the I20 model, whereas those surrounded by gray lines show the results from assuming a modified blackbody radiation with a typical dust temperature (i.e., $T_{\rm dust} = 50$ K). Right: D/G against the gas-phase metallicity. Our fiducial constraints from $M_{\rm gas} = M_{\rm dyn}$–$M_*$ are shown with the red star and brown hexagon, while those from $M_{\rm gas} = 0.1$, 0.5, and 0.9 ($M_{\rm gas} + M_*$) are illustrated with the red and brown shaded regions with different levels of opacity. Observational constraints at $z = 2$–8 (G. E. Magdis et al. 2012; G. Popping et al. 2023; F. Valentino et al. 2024; H. Algera et al. 2026) and a model (G. Popping et al. 2017) are shown in colors depending on their redshift. The black solid line and circles indicate the median relation and observations at $z = 0$ (A. Rémy-Ruyer et al. 2014).

from the dynamical masses (see also S. Schouws et al. 2025a). For instance, the [C II] line can be detected over 3–15 hr source integration in the case of $f_{\rm gas} \sim 0.9$, based on the calibration of $L_{\rm [CII]}/M_{\rm mol}$ in A. Zanella et al. (2018).[20]

In addition to grain growth, dust destruction can play a critical role, particularly from SN reverse shocks. Figure 4 shows the evolution of stellar and dust masses from SNe and AGB stars, based on each galaxy's SFH, derived using BAGPIPES or PROSPECTOR (S. Carniani et al. 2025; Y. Harikane et al. 2025; J. A. Zavala et al. 2025; see also Section 2). The SFHs are parameterized with an exponential profile (SFR(t) $\propto \exp(t/\tau)$) with star formation starting at $z = 20$ and with a delayed-τ profile (SFR(t) $\propto t \times \exp(t/\tau)$) with star formation starting at $z = 30$ for GHZ2 and for GS-z14-0, respectively. Our predictions are based on a recipe presented in R. Valiante et al. (2009; see also R. Schneider & R. Maiolino 2024 for a recent review), with the SN dust yield from S. Bianchi & R. Schneider (2007) and S. Zhukovska et al. (2008) and the AGB dust yield from A. S. Ferrarotti & H. P. Gail (2006) and the ATON code (F. Dell'Agli et al. 2019). Given the metal-poor nature of the galaxies at $z > 12$, we use the dust yield model with a metallicity of 10^{-4}–$0.1\,Z_\odot$. We integrate the dust yield from stars ranging over 0.1–100 $M_\odot$ under a Larson (R. B. Larson 1998) IMF with $\alpha = 1.35$ and $M_{\rm ch} = 0.35$, which is similar to a Salpeter IMF (E. E. Salpeter 1955).

Given the young stellar ages derived from SED fitting ($\lesssim$150 Myr) and the age of the Universe at these redshifts ($\lesssim$300 Myr), dust from SNe dominates the bulk mass. For both GHZ2 and GS-z14-0, dust destruction by SN reverse shocks might not necessarily be significant (see Figure 4). If the dust destruction efficiency does not change significantly between $z \sim 7$ and $z \sim 12$, the difference in $M_{\rm dust}/M_*$ is simply explained by the efficient ISM grain growth with $\tau_{\rm acc} \sim 5$–100 Myr, given their longer ages of tens to hundreds of Myr compared to our $z > 12$ systems. We note that several studies suggest that dust destruction can be efficient in metal-poor conditions (T. Nozawa et al. 2007; F. D. Priestley et al. 2022) and that inefficient dust destruction or high condensation efficiency may play a more important role in $z \sim 7$ galaxies (P. Dayal et al. 2022; M. Palla et al. 2024).

4.2. SFE

In this section, we compare the efficiencies of the gas consumption at $z > 12$ with those at $z < 9$. In our fiducial calculations, the total gas masses of the target galaxies are computed as $M_{\rm gas} = M_{\rm dyn}$–$M_*$, as outlined in Section 4.1, and following M. Aravena et al. (2024) we assume the ISM is dominated by the molecular gas ($M_{\rm gas} \simeq M_{\rm mol}$). As in Section 4.1, we also calculate gas masses assuming $f_{\rm gas} = 0.1$–0.9. The caveats associated with these assumptions will be discussed below. On the other hand, we calculate the SFRs by averaging the nonparametric SFHs over timescales of 10 Myr and 100 Myr (Table 1).

Figure 5 illustrates the evolution of the SFE, defined as SFR/$M_{\rm mol}$. For comparison, we plot data from MS and "SB" galaxies from PHIBSS (L. J. Tacconi et al. 2018), from lensed low-mass galaxies at $z \sim 2$ (M. Dessauges-Zavadsky et al. 2015), from lensed dusty star-forming galaxies (DSFGs; M. Aravena et al. 2016; S. Jarugula et al. 2021; J. A. Zavala et al. 2022), from unlensed DSFGs (J. E. Birkin et al. 2021),

[20] The calibration in A. Zanella et al. (2018) does not cover the metallicity range of $Z \lesssim 0.2\,Z_\odot$ (see also A. Rémy-Ruyer et al. 2014). The estimation of the [C II] line luminosity here may be optimistic, as the [C II] line is likely to be fainter in low-Z galaxies (e.g., T. Hashimoto et al. 2019; Y. Harikane et al. 2020; T. J. L. C. Bakx et al. 2024).

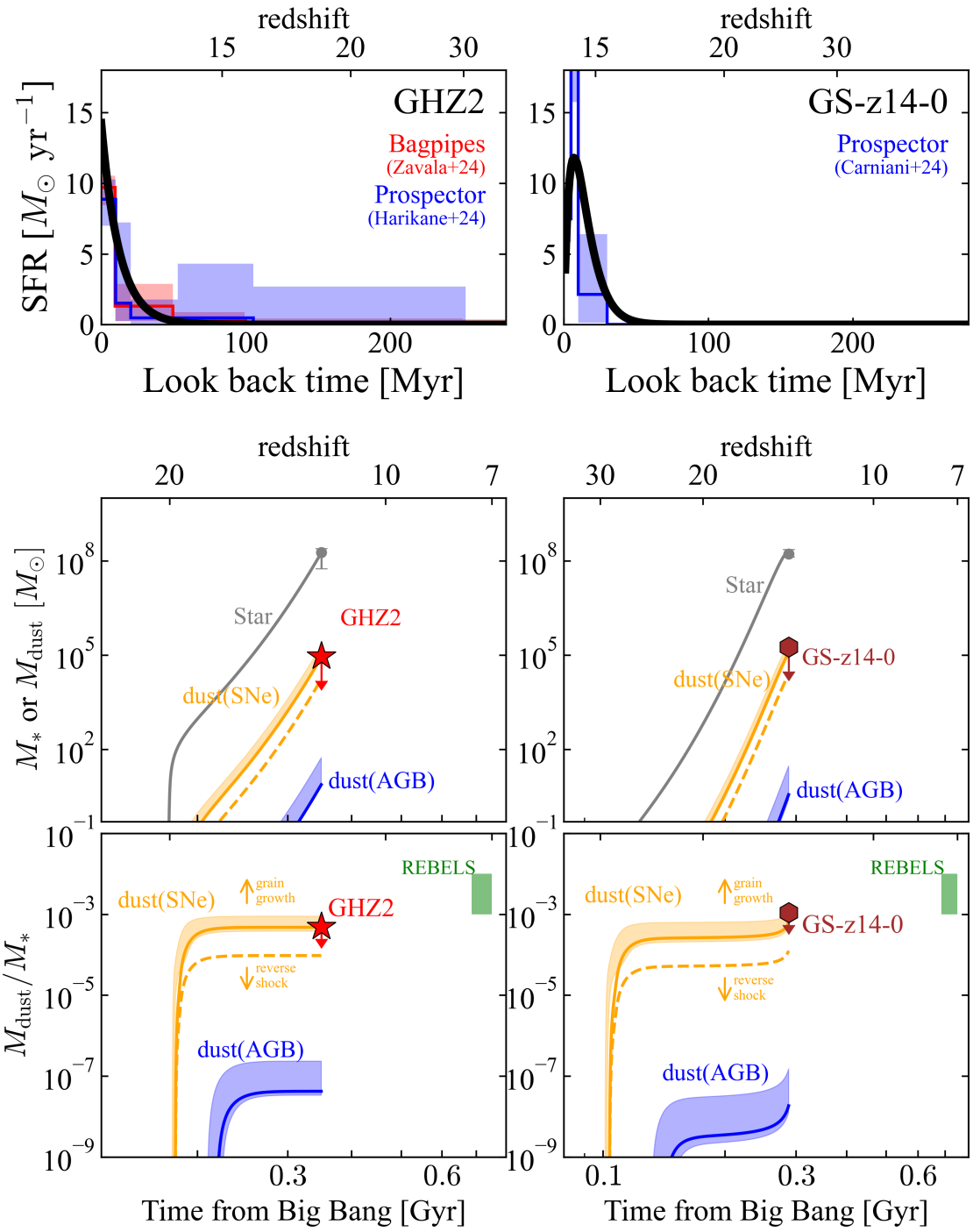

Figure 4. Dust and SFHs derived from nonparametric SFH and SN/AGB dust yield models for GHZs (left) and GS-z14-0 (right). Top: smoothed exponentially rising SFH (black) derived from BAGPIPES (red; J. A. Zavala et al. 2025) and PROSPECTOR (blue; S. Carniani et al. 2025; Y. Harikane et al. 2025). Middle and bottom: our constraints on the dust mass with the previous results from the REBELS survey (P. Dayal et al. 2022; A. Ferrara et al. 2022; M. W. Topping et al. 2022). The models of the dust production history from the SFH are based on R. Valiante et al. (2009), with the SN dust yield from S. Bianchi & R. Schneider (2007) and S. Zhukovska et al. (2008) and the AGB dust yield from A. S. Ferrarotti & H. P. Gail (2006) and the ATON code (F. Dell'Agli et al. 2019). For the S. Zhukovska et al. (2008) and ATON models, we show ranges of 10^{-4}–0.1 $Z_\odot$ with the orange and blue shaded regions. The effects of the IMF and reverse shock are shown by two arrows. The SN yield from the S. Bianchi & R. Schneider (2007) model with a 20% dust survival fraction is shown with the orange dashed line.

from ALPINE (M. Dessauges-Zavadsky et al. 2020), and from REBELS (M. Aravena et al. 2024). We also show the scaling relations from L. J. Tacconi et al. (2020) and N. Scoville et al. (2017) at the stellar mass of $M_* = 10^{10}\,M_\odot$. While the range of the stellar masses at each redshift spread over $\log M_*/M_\odot = 8$–11 (with high-redshift galaxies showing systematically smaller stellar masses), the dependence of the SFE on the stellar mass is small ($\propto 1/10^{0.01-0.03}$). Also, it is worth noting that molecular gas tracers differ across studies (CO in PHIBSS and sub-millimeter galaxies, and [C II] in ALPINE and REBELS), but these variations do not introduce systematic uncertainties into the dynamical mass-based

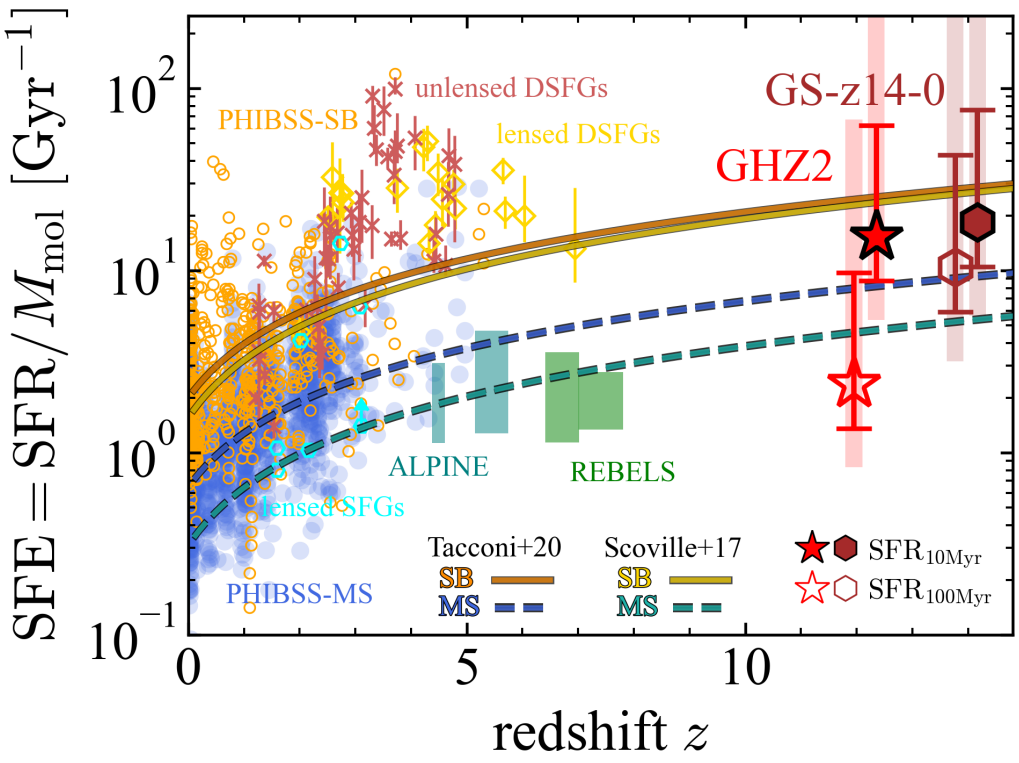

Figure 5. Redshift evolution of the SFE. Our fiducial calculations (the red stars and brown hexagons) are shown, based on $\mathrm{SFR}_{\rm 10Myr}$ (filled markers) and $\mathrm{SFR}_{\rm 100Myr}$ (open markers), respectively. We also illustrate the SFEs based on the gas masses assuming $f_{\rm gas} = 0.1$–0.9 with the red and brown shaded regions associated with the markers. Shifts have been added in the x-axis direction for ease of viewing. Previous studies of the MS galaxies from PHIBSS (blue circles; L. J. Tacconi et al. 2018), lensed low-mass star-forming galaxies at $z \sim 2$ (cyan hexagons; M. Dessauges-Zavadsky et al. 2015), galaxies from ALPINE (blue shades; M. Dessauges-Zavadsky et al. 2020), and galaxies from REBELS (green shades; M. Aravena et al. 2024), as well as SB galaxies from PHIBSS (orange circles), unlensed DSFGs (brown crosses; J. E. Birkin et al. 2021), and lensed DSFGs (yellow diamonds; M. Aravena et al. 2016; S. Jarugula et al. 2021; J. A. Zavala et al. 2022), are also plotted. The predicted evolutions from L. J. Tacconi et al. (2020; orange solid and blue dashed lines) and N. Scoville et al. (2017; yellow solid and green dashed lines) are also plotted.

estimations (M. Dessauges-Zavadsky et al. 2020; J. E. Birkin et al. 2021; M. Aravena et al. 2024).

For GHZ2, the SFR averaged over 100 Myr, $\mathrm{SFR}_{\rm 100\,Myr}$, is smaller than $\mathrm{SFR}_{\rm 10\,Myr}$, owing to its inferred rapidly increasing star formation activity (see Figure 4). GS-z14-0 has comparable SFRs between the 10 Myr timescale and the 100 Myr timescale. The SFEs of GHZ2 and GS-z14-0 for the 10 Myr timescale are $\mathrm{SFE}_{\rm 10\,Myr} \gtrsim 10\,\mathrm{Gyr}^{-1}$ and are in good agreement with the extrapolated redshift evolution of SB galaxies. This contrasts with the UV-bright galaxies at $z = 4$–8 selected via the Lyman break method, which have SFEs of $\sim$1 Gyr^{-1} and follow the MS scaling relation or even prefer a shallower evolution (M. Dessauges-Zavadsky et al. 2020; M. Aravena et al. 2024). Indeed, this high SFE in GHZ2 is in line with the interpretation in J. A. Zavala et al. (2024) of the H II-galaxy-like nature of GHZ2.

The timescales over which the star formation is being calculated can be important when comparing our measurements with those at lower redshifts. In Figure 5, the SFRs of UV-selected galaxies at $z = 4$–8 (i.e., ALPINE/REBELS galaxies) are calculated from the rest-frame UV and IR continuum tracing the average star formation activity over $\sim$100 Myr. Indeed, R. Endsley et al. (2024) reported that around 10% of $z \approx 6$–9 UV-bright galaxies with $M_{\rm UV} \sim -20$ mag show an order of magnitude higher SFR over $<$10 Myr. Therefore, $\sim$10% of the ALPINE/REBELS galaxies may have an order of magnitude larger SFR over a $<$10 Myr timescale, implying a higher SFR, in better agreement with the SB scaling relation.[21] On the other hand, as described above, both GHZ2 and GS-z14-0 are likely under an SB episode, which may suggest that this "SB" phase with efficient gas consumption is more ubiquitous among UV-bright galaxies at $z > 12$ than at $z \sim 6$.

GHZ2 and GS-z14-0 show comparable fractions of molecular gas mass within the baryonic content ($M_{\rm gas}/(M_* + M_{\rm gas}) \sim 0.5$–$0.7$; see also S. Carniani et al. 2025) as those of the LBGs at $z = 4$–8 ($M_{\rm gas}/M_* \sim 1$ M. Dessauges-Zavadsky et al. 2020; M. Aravena et al. 2024). Their instantaneous high SFEs and high gas fractions may be the result of a bursty SFH, which increases the visibility of UV-bright galaxies during short and intense bursts of star formation (e.g., G. Sun et al. 2023; A. Kravtsov & V. Belokurov 2024). Approximating $M_{\rm gas} \approx f_b M_{\rm halo}$, where f_b and $M_{\rm halo}$ are the cosmic baryon fraction and the host halo mass, respectively, the stellar-to-halo mass ratio ($\epsilon_* = M_*/M_{\rm halo}$) becomes around 0.3, which is consistent with recent

[21] The fraction of galaxies having rising SFHs may increase for galaxies with small absolute UV magnitude (Y. Asada et al. 2024; R. Endsley et al. 2024; Y. Harikane et al. 2025). As the ALPINE and REBELS galaxies have smaller absolute UV magnitude ($M_{\rm UV} \sim -21$ to -22 mag) than those of R. Endsley et al. (2024; $M_{\rm UV} \sim -20$ mag), the fraction of the galaxies lying on the SB sequence over a 10 Myr timescale may be higher than $\sim$10% for the ALPINE and REBELS galaxies. However, at least not every such galaxy has a rising SFH (M. W. Topping et al. 2022; M. Palla et al. 2024).

observations (e.g., C. M. Casey et al. 2024; M. Shuntov et al. 2025) and models (e.g., R. S. Somerville et al. 2025; L. Y. A. Yung et al. 2025) implying high ϵ_* in the galaxies residing in the most massive halos at each epoch. Further observations capturing the rest-frame optical stellar continuum will enable us to make more accurate constraints on the stellar mass and, therefore, on the gas fraction.

One major caveat in using $M_{\rm dyn}$–M_* as a proxy of $M_{\rm gas}$ is the uncertain fraction of the molecular gas within the total gas. However, if the molecular gas fraction is below unity, the derived $M_{\rm mol}$ decreases and the SFE increases. Therefore, the adopted molecular gas fraction does not affect our conclusion. We acknowledge, however, that conducting direct observations of cold ISM tracers, such as [C II] or CO lines, is crucial to putting better constraints on the molecular gas mass. As shown in the shaded boxes in Figure 5, the assumption of the $f_{\rm gas}$ range of 0.1–0.9 prevents the imposing of any meaningful constraints on the SFE. Recent ALMA observations targeting [C II]158 μm at GS-z14-0 (S. Schouws et al. 2025a) reported a molecular gas mass upper limit of $M_{\rm mol} < 1.6 \times 10^9\,M_\odot$, consistent with the dynamical estimation ($M_{\rm gas} = 5.4^{+4.1}_{-4.0} \times 10^8\,M_\odot$). Experiments involving the detection of [C II] from deeper observations will be important keys to confirming or ruling out our conclusion.

5. Summary

In this paper, we have investigated the dust and gas content of the brightest galaxies at $z > 12$—GHZ2 and GS-z14-0—based on direct ALMA observations that trace the bulk of the dust mass in these galaxies. From the combination of ultradeep ALMA observations and an analytical thermal equilibrium model, we have found:

1. The 3σ upper limits on the dust continuum at $\lambda_{\rm rest} = 88\,\mu$m are 10.3 μJy and 14.9 μJy for the Band-6 observations of GHZ2 and GS-z14-0, respectively. Combining these observations with an analytical model based on thermal equilibrium and clumpy dust geometry (I20), we derived dust mass upper limits of $\log M_{\rm dust}/M_\odot < 5.0$ and <5.3, respectively.
2. The comparison of our constraints on the M_*–$M_{\rm dust}$ plane and dust production models at $z > 4$ does not imply efficient dust grain growth with extreme condensation efficiency $f_{\rm cond}$. Assuming most massive galaxies at $z > 12$ are potential progenitors of most massive galaxies at $z = 7$, a short accretion timescale scenario with $\tau_{\rm acc} \sim$ 5–100 Myr, as in H.-M. Liu & H. Hirashita (2019), is supported, rather than a high-$f_{\rm cond}$ scenario.
3. Given the very young ages of the target galaxies, dust yields from AGB stars and grain growth are not likely to be effective. The upper limits on the dust-to-stellar mass ratios of the two $z > 12$ galaxies are barely consistent with SN dust formation models without any dust destruction.
4. Based on the gas masses from $M_{\rm gas} = M_{\rm dyn}$–$M_*$ and SFHs, we inferred SFEs over the past 10 Myr, which reach high values above $\sim$10 Gyr^{-1}, comparable with the predicted SFE evolution for SB galaxies. Both GHZ2 and GS-z14-0 may exhibit short SB-like episodes only for relatively short periods of up to $\sim$10–30 Myr. From a comparison with UV-bright galaxies at $z \sim 6$, we hypothesize that such "SB" activity may be more ubiquitous in UV-bright galaxies at $z > 12$ than at $z \sim 6$, potentially due to bursty SFHs (e.g., G. Sun et al. 2023).

Our study demonstrates the importance of observing cold ISM tracers, such as dust continuum and [C II] line observations with ALMA, to derive the current and future star formation activity of UV-bright galaxies. Since our analysis with the thermal equilibrium model predicts very high $T_{\rm dust}$, further deep ALMA observations at high frequency to capture near the peak of the dust thermal emission will be useful for identifying dust at $z > 12$. For instance, $\sim$30 hr ALMA Band-9 observations covering rest frame $\sim$30 μm will allow us to add tighter constraints on $M_{\rm dust}$ in the $T_{\rm dust} > 100$ K regime. To further understand the emergence of dust across the Universe, investigating the gas and dust content of the most massive galaxies at $z \sim$ 8–11 is necessary to constrain the grain growth in the ISM. Systematic comparison of ISM conditions, such as the gas/electron density, across the Universe might be critical to understanding the origin of the lack of dust and the potential "SB" nature of $z > 12$ galaxies.

Acknowledgments

We thank the anonymous referee for constructive comments and suggestions for improving this manuscript. We thank P. Dayal for providing us with data from their semianalytical calculation. This paper makes use of the following ALMA data: ADS/JAO.ALMA#2021.A.00020.S, #2023.A.00017, and #2023.A.00037. ALMA is a partnership of ESO (representing its member states), NSF (USA) and NINS (Japan), together with NRC (Canada), MOST and ASIAA (Taiwan), and KASI (Republic of Korea), in cooperation with the Republic of Chile. The Joint ALMA Observatory is operated by ESO, AUI/NRAO, and NAOJ. I.M. and A.K.I. acknowledge support from NAOJ ALMA Scientific Research grant No. 2020-16B. The authors acknowledge the GLASS and JADES teams led by Tommaso Treu and Daniel Eisenstein and Nora Luetzgendorf, respectively, for developing their observing programs. The JWST data presented in this article were obtained from the Mikulski Archive for Space Telescopes (MAST) at the Space Telescope Science Institute. The specific observations analyzed can be found at MAST via doi:10.17909/wz7w-2208. J.A.Z. acknowledges funding from JSPS KAKENHI grant No. KG23K13150. The data analysis was in part carried out using the Multi-wavelength Data Analysis System operated by the Astronomy Data Center (ADC), National Astronomical Observatory of Japan. K.K. acknowledges support from the Knut and Alice Wallenberg Foundation (KAW 2020.0081). P.S. acknowledges INAF Mini grant 2022, "The evolution of passive galaxies through cosmic time."

ORCID iDs

Ikki Mitsuhashi https://orcid.org/0000-0001-7300-9450
Jorge A. Zavala https://orcid.org/0000-0002-7051-1100
Akio K. Inoue https://orcid.org/0000-0002-7779-8677
Marco Castellano https://orcid.org/0000-0001-9875-8263
Antonello Calabrò https://orcid.org/0000-0003-2536-1614
Caitlin M. Casey https://orcid.org/0000-0002-0930-6466
Maximilien Franco https://orcid.org/0000-0002-3560-8599

Bunyo Hatsukade https://orcid.org/0000-0001-6469-8725
Nimish P. Hathi https://orcid.org/0000-0001-6145-5090
Ryota Ikeda https://orcid.org/0000-0002-2634-9169
Anton M. Koekemoer https://orcid.org/0000-0002-6610-2048
Jeyhan Kartaltepe https://orcid.org/0000-0001-9187-3605
Kirsten K. Knudsen https://orcid.org/0000-0002-7821-8873
Paola Santini https://orcid.org/0000-0002-9334-8705
Roberto Terlevich https://orcid.org/0000-0001-6774-3499
L. Y. Aaron Yung https://orcid.org/0000-0003-3466-035X

References

Algera, H., Rowland, L., Stefanon, M., et al. 2026, MNRAS, 545, staf1897
Algera, H. S. B., Inami, H., Sommovigo, L., et al. 2024, MNRAS, 527, 6867
Aravena, M., Heintz, K., Dessauges-Zavadsky, M., et al. 2024, A&A, 682, A24
Aravena, M., Spilker, J. S., Bethermin, M., et al. 2016, MNRAS, 457, 4406
Asada, Y., Sawicki, M., Abraham, R., et al. 2024, MNRAS, 527, 11372
Asano, R. S., Takeuchi, T. T., Hirashita, H., & Inoue, A. K. 2013, EP&S, 65, 213
Atek, H., Shuntov, M., Furtak, L. J., et al. 2023, MNRAS, 519, 1201
Austin, D., Conselice, C. J., Adams, N. J., et al. 2025, ApJ, 995, 43
Bakx, T. J. L. C., Algera, H. S. B., Venemans, B., et al. 2024, MNRAS, 532, 2270
Bakx, T. J. L. C., Sommovigo, L., Carniani, S., et al. 2021, MNRAS, 508, L58
Bakx, T. J. L. C., Tamura, Y., Hashimoto, T., et al. 2020, MNRAS, 493, 4294
Bakx, T. J. L. C., Zavala, J. A., Mitsuhashi, I., et al. 2023, MNRAS, 519, 5076
Bendo, G. J., Wilson, C. D., Warren, B. E., et al. 2010, MNRAS, 402, 1409
Bergamini, P., Acebron, A., Grillo, C., et al. 2023, ApJ, 952, 84
Bianchi, S., & Schneider, R. 2007, MNRAS, 378, 973
Birkin, J. E., Weiss, A., Wardlow, J. L., et al. 2021, MNRAS, 501, 3926
Bouwens, R., Illingworth, G., Oesch, P., et al. 2023, MNRAS, 523, 1009
Burgarella, D., Buat, V., Theulé, P., et al. 2024, arXiv:2410.23959
Calabro, A., Castellano, M., Zavala, J. A., et al. 2024, ApJ, 975, 245
Carnall, A. C., McLure, R. J., Dunlop, J. S., & Davé, R. 2018, MNRAS, 480, 4379
Carniani, S., D'Eugenio, F., Ji, X., et al. 2025, A&A, 696, A87
Carniani, S., Hainline, K., D'Eugenio, F., et al. 2024, Natur, 633, 318
CASA Team, Bean, B., Bhatnagar, S., et al. 2022, PASP, 134, 114501
Casey, C. M. 2012, MNRAS, 425, 3094
Casey, C. M., Akins, H. B., Shuntov, M., et al. 2024, ApJ, 965, 98
Castellano, M., Fontana, A., Treu, T., et al. 2022, ApJL, 938, L15
Castellano, M., Napolitano, L., Fontana, A., et al. 2024, ApJ, 972, 143
Chávez, R., Terlevich, R., Terlevich, E., et al. 2014, MNRAS, 442, 3565
Ciesla, L., Boquien, M., Boselli, A., et al. 2014, A&A, 565, A128
Cullen, F., McLeod, D. J., McLure, R. J., et al. 2024, MNRAS, 531, 997
Cullen, F., McLure, R. J., McLeod, D. J., et al. 2023, MNRAS, 520, 14
Curti, M., Maiolino, R., Curtis-Lake, E., et al. 2024, A&A, 684, A75
da Cunha, E., Hodge, J. A., Casey, C. M., et al. 2021, ApJ, 919, 30
da Cunha, E., Walter, F., Smail, I. R., et al. 2015, ApJ, 806, 110
Dayal, P., Ferrara, A., Sommovigo, L., et al. 2022, MNRAS, 512, 989
de Bennassuti, M., Schneider, R., Valiante, R., & Salvadori, S. 2014, MNRAS, 445, 3039
Dell'Agli, F., Valiante, R., Kamath, D., Ventura, P., & García-Hernández, D. A. 2019, MNRAS, 486, 4738
Dessauges-Zavadsky, M., Ginolfi, M., Pozzi, F., et al. 2020, A&A, 643, A5
Dessauges-Zavadsky, M., Zamojski, M., Schaerer, D., et al. 2015, A&A, 577, A50
Di Cesare, C., Graziani, L., Schneider, R., et al. 2023, MNRAS, 519, 4632
Draine, B. T. 1990, ASPC, 12, 193
Draine, B. T. 2009, ASPC, 414, 453
Draine, B. T., Dale, D. A., Bendo, G., et al. 2007, ApJ, 663, 866
Dwek, E. 1998, ApJ, 501, 643
Dwek, E., & Scalo, J. M. 1980, ApJ, 239, 193
Endsley, R., Stark, D. P., Whitler, L., et al. 2024, MNRAS, 533, 1111
Ferrara, A. 2024, A&A, 684, A207
Ferrara, A., Carniani, S., di Mascia, F., et al. 2025a, A&A, 694, A215
Ferrara, A., Pallottini, A., & Sommovigo, L. 2025b, A&A, 694, A286
Ferrara, A., Sommovigo, L., Dayal, P., et al. 2022, MNRAS, 512, 58
Ferrarotti, A. S., & Gail, H. P. 2006, A&A, 447, 553
Finkelstein, S. L., Leung, G. C. K., Bagley, M. B., et al. 2024, ApJL, 969, L2
Fudamoto, Y., Inoue, A. K., & Sugahara, Y. 2023, MNRAS, 521, 2962
Galliano, F., Dwek, E., & Chanial, P. 2008, ApJ, 672, 214
Graziani, L., Schneider, R., Ginolfi, M., et al. 2020, MNRAS, 494, 1071
Harikane, Y., Inoue, A. K., Ellis, R. S., et al. 2025, ApJ, 980, 138
Harikane, Y., Ouchi, M., Inoue, A. K., et al. 2020, ApJ, 896, 93
Harikane, Y., Ouchi, M., Oguri, M., et al. 2023, ApJS, 265, 5
Hashimoto, T., Inoue, A. K., Mawatari, K., et al. 2019, PASJ, 71, 71
Helton, J. M., Rieke, G. H., Alberts, S., et al. 2025, NatAs, 9, 729
Hirashita, H., Tajiri, Y. Y., & Kamaya, H. 2002, A&A, 388, 439
Imara, N., Loeb, A., Johnson, B. D., Conroy, C., & Behroozi, P. 2018, ApJ, 854, 36
Inami, H., Algera, H. S. B., Schouws, S., et al. 2022, MNRAS, 515, 3126
Inoue, A. K. 2011, EP&S, 63, 1027
Inoue, A. K., Hashimoto, T., Chihara, H., & Koike, C. 2020, MNRAS, 495, 1577
Issa, M. R., MacLaren, I., & Wolfendale, A. W. 1990, A&A, 236, 237
Jarugula, S., Vieira, J. D., Weiss, A., et al. 2021, ApJ, 921, 97
Johnson, B. D., Leja, J., Conroy, C., & Speagle, J. S. 2021, ApJS, 254, 22
Kennicutt, R. C., Jr. 1998, ApJ, 498, 541
Kennicutt, R. C., Jr., & De Los Reyes, M. A. C. 2021, ApJ, 908, 61
Kohandel, M., Ferrara, A., Pallottini, A., et al. 2023, MNRAS, 520, L16
Koornneef, J. 1982, A&A, 107, 247
Kravtsov, A., & Belokurov, V. 2024, arXiv:2405.04578
Laporte, N., Ellis, R. S., Boone, F., et al. 2017, ApJL, 837, L21
Larson, R. B. 1998, MNRAS, 301, 569
Leroy, A. K., Bolatto, A., Gordon, K., et al. 2011, ApJ, 737, 12
Li, Q., Narayanan, D., & Davé, R. 2019, MNRAS, 490, 1425
Lisenfeld, U., & Ferrara, A. 1998, ApJ, 496, 145
Liu, H.-M., & Hirashita, H. 2019, MNRAS, 490, 540
Magdis, G. E., Daddi, E., Béthermin, M., et al. 2012, ApJ, 760, 6
Magrini, L., Bianchi, S., Corbelli, E., et al. 2011, A&A, 535, A13
Mancini, M., Schneider, R., Graziani, L., et al. 2015, MNRAS, 451, L70
Mauerhofer, V., & Dayal, P. 2023, MNRAS, 526, 2196
Mitsuhashi, I., Harikane, Y., Bauer, F. E., et al. 2024, ApJ, 971, 161
Naidu, R. P., Oesch, P. A., van Dokkum, P., et al. 2022, ApJL, 940, L14
Nakajima, K., Ouchi, M., Isobe, Y., et al. 2023, ApJS, 269, 33
Nozawa, T., Kozasa, T., Habe, A., et al. 2007, ApJ, 666, 955
Ono, Y., Harikane, Y., Ouchi, M., et al. 2023, ApJ, 951, 72
Palla, M., De Looze, I., Relaño, M., et al. 2024, MNRAS, 528, 2407
Popping, G., Shivaei, I., Sanders, R. L., et al. 2023, A&A, 670, A138
Popping, G., Somerville, R. S., & Galametz, M. 2017, MNRAS, 471, 3152
Priestley, F. D., De Looze, I., & Barlow, M. J. 2022, MNRAS, 509, L6
Rémy-Ruyer, A., Madden, S. C., Galliano, F., et al. 2014, A&A, 563, A31
Robertson, B., Johnson, B. D., Tacchella, S., et al. 2024, ApJ, 970, 31
Salpeter, E. E. 1955, ApJ, 121, 161
Sanders, D. B., Scoville, N. Z., & Soifer, B. T. 1991, ApJ, 370, 158
Santini, P., Maiolino, R., Magnelli, B., et al. 2014, A&A, 562, A30
Sargent, M. T., Béthermin, M., Daddi, E., & Elbaz, D. 2012, ApJL, 747, L31
Schneider, R., Hunt, L., & Valiante, R. 2016, MNRAS, 457, 1842
Schneider, R., & Maiolino, R. 2024, A&ARv, 32, 2
Schouws, S., Bouwens, R. J., Algera, H., et al. 2025a, ApJ, 988, 19S
Schouws, S., Bouwens, R. J., Ormerod, K., et al. 2025b, ApJ, 988, 19
Scoville, N., Lee, N., Vanden Bout, P., et al. 2017, ApJ, 837, 150
Shuntov, M., Ilbert, O., Toft, S., et al. 2025, A&A, 695, A20
Somerville, R. S., Yung, L. Y. A., Lancaster, L., et al. 2025, MNRAS, 544, 3774
Sommovigo, L., Ferrara, A., Carniani, S., et al. 2022b, MNRAS, 517, 5930
Sommovigo, L., Ferrara, A., Pallottini, A., et al. 2022a, MNRAS, 513, 3122
Sun, G., Faucher-Giguère, C.-A., Hayward, C. C., et al. 2023, ApJL, 955, L35
Tacconi, L. J., Genzel, R., Saintonge, A., et al. 2018, ApJ, 853, 179
Tacconi, L. J., Genzel, R., & Sternberg, A. 2020, ARA&A, 58, 157
Tamura, Y., Mawatari, K., Hashimoto, T., et al. 2019, ApJ, 874, 27
Todini, P., & Ferrara, A. 2001, MNRAS, 325, 726
Topping, M. W., Stark, D. P., Endsley, R., et al. 2022, MNRAS, 516, 975
Treu, T., Roberts-Borsani, G., Bradac, M., et al. 2022, ApJ, 935, 110
Valentino, F., Fujimoto, S., Giménez-Arteaga, C., et al. 2024, A&A, 685, A138
Valiante, R., Schneider, R., Bianchi, S., & Andersen, A. C. 2009, MNRAS, 397, 1661
Vijayan, A. P., Clay, S. J., Thomas, P. A., et al. 2019, MNRAS, 489, 4072
Witstok, J., Jones, G. C., Maiolino, R., Smit, R., & Schneider, R. 2023a, MNRAS, 523, 3119
Witstok, J., Shivaei, I., Smit, R., et al. 2023b, Natur, 621, 267

Witstok, J., Smit, R., Maiolino, R., et al. 2022, MNRAS, 515, 1751
Yang, L., Morishita, T., Leethochawalit, N., et al. 2022, ApJL, 938, L17
Yoon, I., Carilli, C. L., Fujimoto, S., et al. 2023, ApJ, 950, 61
Yung, L. Y. A., Somerville, R. S., Finkelstein, S. L., Wilkins, S. M., & Gardner, J. P. 2024, MNRAS, 527, 5929
Yung, L. Y. A., Somerville, R. S., & Iyer, K. G. 2025, MNRAS, 543, 3802
Zanella, A., Daddi, E., Magdis, G., et al. 2018, MNRAS, 481, 1976
Zavala, J. A., Bakx, T., Mitsuhashi, I., et al. 2024, ApJL, 977, L9
Zavala, J. A., Casey, C. M., Spilker, J., et al. 2022, ApJ, 933, 242
Zavala, J. A., Castellano, M., Akins, H. B., et al. 2025, NatAs, 9, 155
Zhukovska, S. 2014, A&A, 562, A76
Zhukovska, S., Gail, H. P., & Trieloff, M. 2008, A&A, 479, 453